Acta Geophysica (2019) 67:557–575
https://doi.org/10.1007/s11600-019-00274-6

RESEARCH ARTICLE - APPLIED GEOPHYSICS

Prediction of porosity and gas saturation for deep-buried sandstone reservoirs from seismic data using an improved rock-physics model

Yaneng Luo[1] · Handong Huang[1] · Morten Jakobsen[2] · Yadi Yang[3] · Jinwei Zhang[4] · Yanjie Cai[5]

Received: 5 December 2018 / Accepted: 23 February 2019 / Published online: 2 March 2019

Abstract

In recent years, many important discoveries have been made in global deep oil and gas exploration, which indicates that deep exploration has gradually become one of the most important areas in current and future hydrocarbon exploration. However, the prediction of deep reservoirs is very challenging due to their low porosity and complex pore structure characteristics caused by the burial depth and diagenesis. Rock physics provides a link between the geologic reservoir parameters and seismic elastic properties and has evolved to become a key tool of quantitative seismic interpretation. Based on the mineral component and pore structure analysis of studied rocks, we propose an improved rock-physics model by introducing a third feldspar-related pore for deep-buried sandstone reservoirs to the traditional Xu–White model. This modelling process consists of three steps: first, rock matrix modelling using time-average equations; second, dry rock modelling using a multi-pore analytical approximation; and third, fluid-saturated rock modelling using a patchy distribution. It has been used in total porosity estimation, S-wave velocity prediction and rock-physics template establishment. The applicability of the improved rock-physics model is verified by a theoretical quartz-water model test and a real data total porosity estimation compared with the traditional Xu–White model and the density method. Then, a rock-physics template is generated by the improved rock-physics model for porosity and gas saturation prediction using seismic data. This template is carefully calibrated and validated by well-log data at both the well-log scale and seismic scale. Finally, the feasibility of the established rock-physics template for porosity and gas saturation prediction is validated by a deep-buried sandstone reservoir application in the East China Sea.

Keywords Deep exploration · Gas-bearing sandstone · Pore structure · Rock-physics modelling · Seismic prediction

Introduction

With the development of deep exploration technologies in both the geological, geophysical theory and engineering, many giant oil and gas fields have been discovered in the world's deep petroliferous basins (Dyman et al. 2003; Dutton and Loucks 2010; Sun et al. 2013; Pang et al. 2015; Lai et al. 2017; Wang et al. 2018; Yuan et al. 2019a). However, the characterization of deep reservoirs is challenging due to the low porosity and complex pore structures caused by the burial depth and diagenesis (Zou et al. 2012; Rezaee et al. 2012; Lai et al. 2016). Rock physics is an effective tool to combine reservoir parameters (porosity, shale volume, fluid saturation, etc.) with seismic elastic parameters (P-wave velocity, S-wave velocity, density, etc.) (Avseth et al. 2005; Mavko et al. 2009; Best 2014). Depending on whether the combination is stepwise or unified, the application workflow may be grouped into two categories: one is

✉ Handong Huang
huanghandongcup@163.com

1 State Key Laboratory of Petroleum Resource and Prospecting, Unconventional Natural Gas Research Institute, China University of Petroleum, Beijing 102249, China

2 Department of Earth Science, University of Bergen, 5020 Bergen, Norway

3 Research Institute of Petroleum Exploration and Development, PetroChina Company Limited, Beijing 100083, China

4 College of Earth Science and Engineering, Shandong University of Science and Technology, Qingdao 266590, Shandong, China

5 Gudao Oil Production Plant of Shengli Oilfield, China Petrochemical Corporation, Dongying 257231, Shandong, China

the sequential or cascaded approach (Buland et al. 2008), and the other is the joint or simultaneous approach (Bosch et al. 2009; Yuan et al. 2019b). Since we mainly focus on the establishment and verification of an improved rock-physics model, we adopt the first cascaded approach to obtain the rock-physics modelling results. Rock-physics models can be used to simulate and infer possible geological scenarios beyond available observation data. They play an important role in both the seismic forward modelling analysis and the quantitative interpretation of seismic inversion results (Avseth et al. 2005).

For high-porosity (larger than 20%) sandstones, combination of granular medium Hertz–Mindlin contact model and Hashin–Shtrikman bounds is often applied to calculate the dry rock moduli under different sorting and cementation trends (Dvorkin and Nur 1996; Ødegaard and Avseth 2004; Mavko et al. 2009; Ruiz and Dvorkin 2009; Avseth et al. 2014). For this type of modelling, the key parameters are the amount and localization of the cement within the grain structure and the coordination number of grains (the average number of contacts per sphere). Since the initial cementation effect will cause a large velocity increase with only a small decrease in porosity, this contact-cement model is often found to overpredict shear stiffnesses in cemented sandstones when the nonuniform contacts and heterogeneous stress are not taken into account (Bachrach and Avseth 2008; Avseth et al. 2010).

For low-porosity sandstones, the influence of pore structure on elastic parameters is more significant than the lithology variation or pore size (Berge et al. 1993; Johansen et al. 2002), which is the main reason for the complex relationship between the elastic parameters and reservoir parameters of deep sandstone reservoirs. The inclusion models (Mavko et al. 2009) can take all these microstructure factors into account and are usually adopted for this kind of modelling. Kuster and Toksöz (1974) derived expressions for the effective elastic moduli by using the long-wavelength first-order scattering theory on the assumption of the noninteraction between inclusions, which means the porosity must be much smaller than the pore aspect ratio. To eliminate this limitation, the differential effective medium (DEM) model calculates the effective elastic moduli by incrementally adding inclusions to the background rock matrix (Norris 1985; Zimmerman 1985; Berryman 1992). This allows the porosity to be higher than the aspect ratio, and the results are always consistent with the rigorous bounds. However, since the system of ordinary differential equations is coupled in the DEM model, the solution must be computed by a numerical iterative process, which will cause tremendous computation time in the real 3D seismic inversion applications. Moreover, for multiple pores, the DEM model is sensitive to the order in which the pores are added to the background rock matrix (Mavko et al. 2009). To overcome these deficiencies of the DEM model, many approximate analytical expressions are made under different assumptions. By assuming the variations of Poisson's ratio caused by the changes of crack porosity are negligible to first order, Berryman, Pride and Wang (2002) deduced the analytical expressions for rocks with dry and saturated cracks. Keys and Xu (2002) decoupled the DEM system by assuming a constant dry rock Poisson's ratio and obtained the analytical dry rock approximation formula, which shows a clear relationship between the elastic parameters and pore parameters and can be easily used for the porosity and pore aspect ratio estimation (Vernik and Kachanov 2010; Bai et al. 2013; Zhao et al. 2013; Keys et al. 2017). Li and Zhang (2012) obtained the analytical expression of the dry rock modulus ratio for different specific pore shapes by assuming the linear relationship between the polarization factors in the DEM system and the modulus ratio. In addition, Jakobsen et al. (2003a, b) derived the common tensor form inclusion model, which can consider other complicated pore microscopic features using the T-matrix method.

The objective of our study is to establish a suitable rock-physics model for porosity and gas saturation prediction of deep-buried sandstone reservoirs. This paper is organized as follows: We first introduce the geological characteristics of studied rocks. Then, we illustrate the theory and methodology of the improved rock-physics model. Next, we apply this model in total porosity estimation, S-wave velocity prediction, and rock-physics template establishment. Next, we use the established template for porosity and gas saturation prediction from real seismic data to demonstrate its performance. Finally, we discuss the parameter calibration rules, the assumptions and uncertainties, and the scale problem by using the improved rock-physics model. Several key conclusions are also drawn at the end of this paper.

Geological setting

The data used in this study are from the East China Sea shelf basin, which is one of the key areas for offshore natural gas exploration in China (Sun et al. 2013). The main target layer is a Paleogene sandstone layer buried more than 4 km depth with an average porosity of 13%. Since the study area is close to the source area, the sandstone has a low compositional maturity and contains unstable feldspar minerals (Hu et al. 2013; Wu et al. 2017). Figure 1 displays the quartz–feldspar–lithic diagram for the Folk's sandstone classification; we observe that the studied sandstone contains an average quartz content of 67.6%, feldspar content of 16.2% and lithic content of 17.2%. The unstable feldspar particles lay a lithologic basis for the development of secondary dissolution pores in deep-buried sandstone reservoirs (Cao et al. 2017).

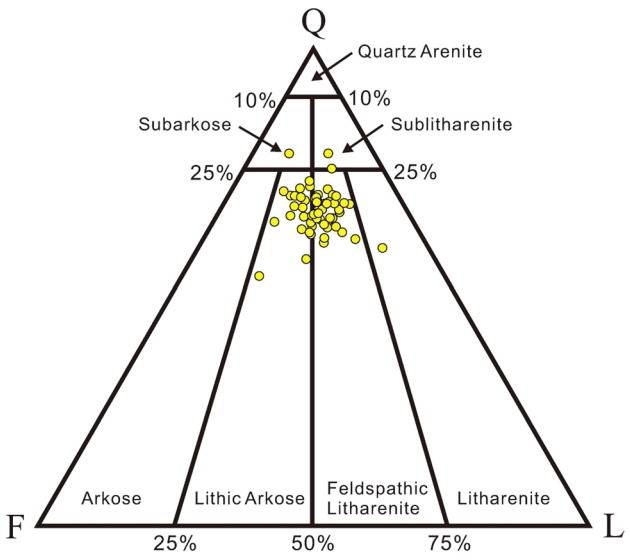

Fig. 1 Quartz–feldspar–lithic (QFL) diagram showing the mineral composition of deep-buried sandstone reservoirs. After Hu et al. (2013)

Figure 2 shows the pore types of deep-buried sandstone reservoirs by scanning electron microscope (SEM) observations. We observe three pore types, which are the primary intergranular pore, the secondary dissolution intragranular and moldic pore, as well as a few microcracks.

The pore characteristics of rocks are closely related to the burial depth and diagenesis (Avseth et al. 2014). As the burial depth increases, the target sandstone layer in the study area has undergone complicated diagenesis, mainly including compaction, cementation and dissolution (Morad et al. 2010; Cao et al. 2017; Lai et al. 2018). Figure 3 displays the diagenesis and pore evolution mode of the target sandstone reservoirs in different stages. Stage I is the mechanical compaction. We see that the primary intergranular porosity decreases rapidly, and the contact pattern of mineral particles shows changes from the point contact to the suture line contact, accompanied by the quartz overgrowth phenomenon. In this stage, the siliceous cement content is low, with an average content of only 0.5% (Hu et al. 2013). As the burial depth increases in stage II, the calcite and clay mineral cements begin to form and fill the intergranular pores (Fig. 2a), which also decreases the porosity. With the further increase in the burial depth in stage III, part of the feldspar particles is dissolved by organic acid, forming secondary pores, including intragranular dissolved pores (Fig. 2b) and moldic pores (Fig. 2c), which greatly improves the reservoir pore space.

Methodology and model test

The extended Xu–White model

According to the above-mentioned geological analysis, the major mineral components of deep-buried low-porosity sandstone reservoirs in the study area are quartz, feldspar and clay. The pore types mainly include primary quartz intergranular semi-stiff pores, secondary feldspar dissolution stiff pores and wet clay soft pores.

Based on the Kuster–Toksöz (1974) and the differential effective medium theories, Xu and White (1995) proposed a clay–sand mixture rock-physics model considering both sand pores and wet clay pores. However, it inherits the defects of the Kuster–Toksöz model and the DEM model, which have low computational efficiency and are sensitive to the pore addition order (Keys and Xu 2002). Here, we extend the Xu–White model by introducing a third type of feldspar-related pores to establish a rock-physics model for deep-buried low-porosity gas-bearing sandstone reservoirs. The modelling process is mainly divided into three steps according to the Xu–White model framework, which includes the modelling of the solid rock matrix, dry rock, and fluid-saturated rock (Fig. 4).

Step 1. Solid rock matrix effective elastic moduli calculation

Following the Xu–White model (1996), we use the time-average equations (Wyllie et al. 1956) to calculate the effective moduli of the solid rock matrix composed of sand grains and clay particles. According to the clastic rock bulk volume formula (Guéguen and Palciauskas 1994),

$$V_S + V_C + \phi = 1, \tag{1}$$

where V_S and V_C represent the sand and clay volume of the whole rock; ϕ is the total porosity. The parameters V_C and ϕ are obtained from well-log data. Then, we can obtain the sand and clay volumes of the rock matrix which are given by:

$$V_C^m = \frac{V_C}{1-\phi}, \tag{2}$$

$$V_S^m = \frac{1-\phi-V_C}{1-\phi}, \tag{3}$$

The P- and S-wave transit time of the rock matrix can be calculated using the time-average equations

$$T_m^p = V_S^m T_S^p + V_C^m T_C^p, \tag{4}$$

$$T_m^s = V_S^m T_S^s + V_C^m T_C^s, \tag{5}$$

and the density of the rock matrix is calculated by

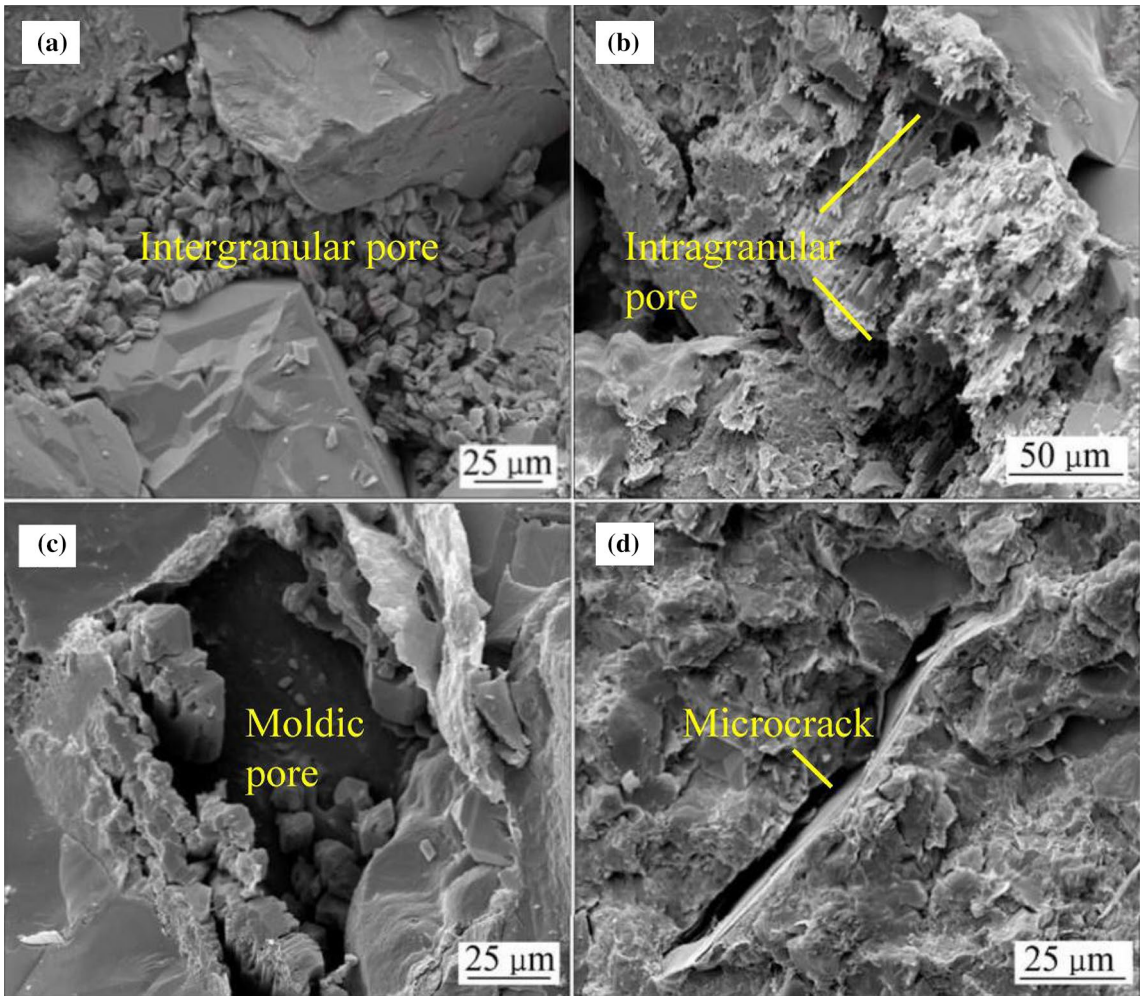

Fig. 2 Pore types of deep-buried sandstone reservoirs by SEM observations (after Cao et al. 2017): **a** primary intergranular pores filled with authigenic kaolinite; **b** secondary feldspar dissolution intragranular pores; **c** secondary feldspar dissolution moldic pores; **d** microcracks

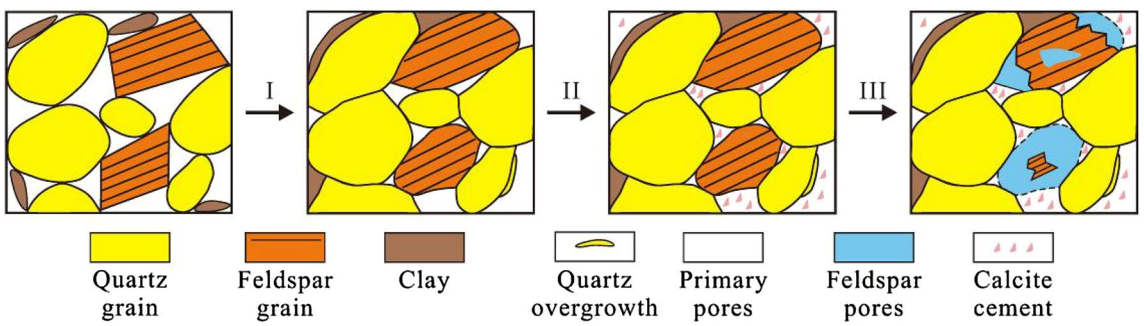

Fig. 3 Diagenesis and pore evolution mode of deep-buried sandstone reservoirs. Stage I represents mechanical compaction, stage II represents early cementation and stage III represents the dissolution of feldspar grains

$$\rho_m = V_S^m \rho_S + V_C^m \rho_C, \tag{6}$$

where T_m^p, T_S^p and T_C^p are the P-wave transit time of the rock matrix, sand and clay, respectively; T_m^s, T_S^s and T_C^s are the corresponding S-wave transit time, respectively; and ρ_m, ρ_S and ρ_C represent the corresponding density, respectively.

Then, the effective bulk modulus K_m and shear modulus μ_m of solid rock matrix can be expressed as

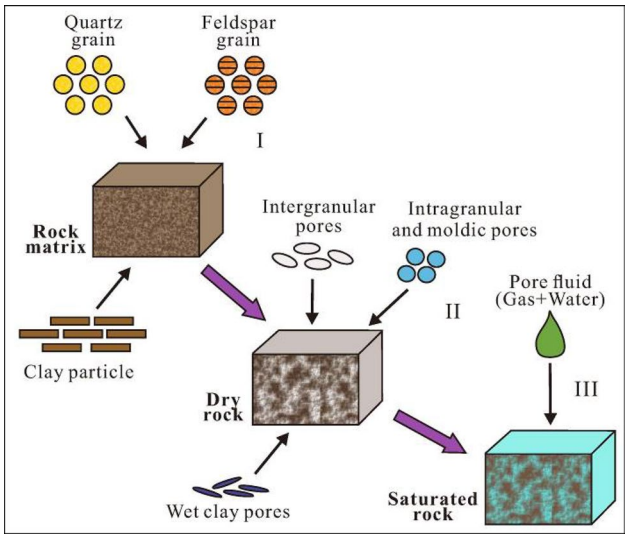

Fig. 4 Schematic diagram of the extended Xu–White model for deep-buried sandstone reservoirs (after Xu and Payne 2009). Step I represents the solid rock matrix modelling, step II represents the dry rock modelling, and step III represents the fluid-saturated rock modelling

$$K_m = \rho_m \left[\left(\frac{1}{T_m^p} \right)^2 - \frac{4}{3} \left(\frac{1}{T_m^s} \right)^2 \right], \tag{7}$$

$$\mu_m = \rho_m \left(\frac{1}{T_m^s} \right)^2. \tag{8}$$

Step 2. Multi-pore dry rock effective elastic moduli calculation

In a two-phase composite, assuming that the host material has elastic moduli K_m and μ_m, and the inclusion material has elastic moduli K_i and μ_i, with porosity ϕ, the effective bulk and shear moduli of this composite $K^*(\phi)$ and $\mu^*(\phi)$ can be obtained by solving the coupled system of ordinary differential equations (Berryman 1992)

$$(1-\phi)\frac{\mathrm{d}}{\mathrm{d}\phi}[K^*(\phi)] = [K_i - K^*(\phi)]P_i^*, \tag{9}$$

$$(1-\phi)\frac{\mathrm{d}}{\mathrm{d}\phi}[\mu^*(\phi)] = [\mu_i - \mu^*(\phi)]Q_i^*, \tag{10}$$

where P_i^* and Q_i^* are the geometric factors associated with Poisson's ratio of the composite and the aspect ratio of the inclusion material, respectively (Keys and Xu 2002; Berryman et al. 2002), and i represents the inclusion phase. The expressions of geometric factors can be easily found in many published papers (Cheng and Toksöz 1979; Xu and White 1995; Keys and Xu 2002).

For the dry rock, $K_i = 0$ and $\mu_i = 0$. Equations (9) and (10) become

$$\frac{\mathrm{d}[K^*(\phi)]}{[K^*(\phi)]\mathrm{d}\phi} = -\frac{P_i^*}{(1-\phi)}, \tag{11}$$

$$\frac{\mathrm{d}[\mu^*(\phi)]}{[\mu^*(\phi)]\mathrm{d}\phi} = -\frac{Q_i^*}{(1-\phi)}. \tag{12}$$

Assuming that the dry rock Poisson's ratio is constant, the geometric factors P_i^* and Q_i^* can be approximated by P_i and Q_i, which are now related to Poisson's ratio of the rock matrix and aspect ratio of the inclusion pores. In this case, the geometric factors are independent of the porosity ϕ, and the ordinary differential equations system can be decoupled (Keys and Xu 2002). Then, integrating Eqs. (11) and (12) within the porosity interval 0 to ϕ_i gives

$$\ln K^*(\phi_i) - \ln K^*(0) = P_i \ln(1-\phi_i), \tag{13}$$

$$\ln \mu^*(\phi_i) - \ln \mu^*(0) = Q_i \ln(1-\phi_i). \tag{14}$$

Combining the initial conditions $K^*(0) = K_m$ and $\mu^*(0) = \mu_m$ with Eqs. (13) and (14), the single-pore dry rock analytical solutions of the effective bulk and shear moduli can be written as

$$K^*(\phi_i) = K_m(1-\phi_i)^{P_i}, \tag{15}$$

$$\mu^*(\phi_i) = \mu_m(1-\phi_i)^{Q_i}. \tag{16}$$

For the multi-pore system of deep-buried sandstone reservoirs, we consider the total pore volume ϕ is composed of quartz intergranular semi-stiff pores ϕ_Q, feldspar dissolution stiff pores ϕ_F and wet clay soft pores ϕ_C; then, we have

$$\phi = \phi_S + \phi_C = \phi_Q + \phi_F + \phi_C \tag{17}$$

Since the porosity of each pore type is proportional to the corresponding mineral content to the first-order approximation (Xu and White 1995), it can be denoted as $\phi_Q = aV_S^m\phi, \phi_F = bV_S^m\phi, \phi_C = V_C^m\phi$, where the coefficients a and b can be obtained from the analysis of rock slices. Finally, the multi-pore dry rock analytical approximation of effective bulk and shear moduli can be expressed as:

$$K^*(\phi) = K_m(1-\phi_Q)^{P_Q}(1-\phi_F)^{P_F}(1-\phi_C)^{P_C} \tag{18}$$

$$\mu^*(\phi) = \mu_m(1-\phi_Q)^{Q_Q}(1-\phi_F)^{Q_F}(1-\phi_C)^{Q_C} \tag{19}$$

Compared with the DEM Eqs. (9) and (10), the multi-pore dry rock analytical approximation Eqs. (18) and (19) are more computationally efficient and are not affected by the addition order of the different pore types.

Step 3. Fluid-saturated rock effective elastic moduli calculation

A fundamental assumption of Gassmann theory is that the pore pressures are equilibrated throughout the pore space (Mavko et al. 2009), which means it is appropriate for rocks with good fluidity and high porosity. However, due to the low porosity and clay–sand mixture background of deep-buried reservoirs in this study area, the pore fluid could have a patchy distribution behaviour (White 1975; Müller et al. 2010; Avseth et al. 2010).

Ignoring attenuation and dispersion caused by the wave-induced fluid flow in porous media, patchy-saturation model (Mavko et al. 2009) calculates the bulk modulus of each fluid phase locally using the Gassmann equation with the shear modulus remaining unchanged. Then, the effective moduli of the patchy-saturated rock can be approximately estimated by the Reuss average. Considering the gas–water two-phase fluid situation, the calculation process can be described by

$$K_{\mathrm{sat},i} = K_{\mathrm{dry}} + \frac{(1 - K_{\mathrm{dry}}/K_m)^2}{\phi/K_{f,i} + (1-\phi)/K_m - K_{\mathrm{dry}}/K_m^2}, \tag{20}$$

$$\mu_{\mathrm{sat}} = \mu_{\mathrm{dry}}, \tag{21}$$

$$M_{\mathrm{sat},i} = K_{\mathrm{sat},i} + \frac{4}{3}\mu_{\mathrm{sat}}, \tag{22}$$

$$M_{\mathrm{sat}} = \left(\frac{S_g}{M_{\mathrm{sat},g}} + \frac{S_w}{M_{\mathrm{sat},w}}\right)^{-1}, \tag{23}$$

where $K_{f,i}$, $K_{\mathrm{sat},i}$ and $M_{\mathrm{sat},i}$ are the bulk modulus, saturated rock bulk modulus and saturated rock compressional modulus of fluid phase i, respectively; K_{dry} and μ_{dry} are the dry rock bulk and shear moduli obtained in step 2; S_g and S_w are gas saturation and water saturation, respectively; and M_{sat} and μ_{sat} are the effective compressional modulus and shear modulus of fluid-saturated rock, respectively.

Finally, from the saturated rock modulus we can calculate the P-wave velocity $V_p = \sqrt{M_{\mathrm{sat}}/\rho_{\mathrm{sat}}}$ and S-wave velocity $V_s = \sqrt{\mu_{\mathrm{sat}}/\rho_{\mathrm{sat}}}$, where the bulk density is given by $\rho_{\mathrm{sat}} = (1-\phi)\rho_m + \phi(S_w\rho_w + S_g\rho_g)$.

Theory model test

To analyse the applicability of the proposed extended Xu–White model and the influence of the pore aspect ratio on elastic parameters, theory model tests of single- and multi-pore type rocks are performed on water–quartz and gas–quartz systems, respectively. We take quartz as the host matrix, having $K_m = 36.6\,\mathrm{GPa}$, $\mu_m = 37\,\mathrm{GPa}$, $\rho_m = 2650\,\mathrm{kg/m^3}$, and water or gas as the pore fluid, having $K_w = 2.5\,\mathrm{GPa}$, $\rho_w = 1020\,\mathrm{kg/m^3}$, $K_g = 0.05\,\mathrm{GPa}$, $\rho_g = 140\,\mathrm{kg/m^3}$ (Mavko et al. 2009). The porosity range is set to 0–0.4. According to the average mean aspect ratios of different pore types defined by Xu and Payne (2009), the pore aspect ratios here are set to $\alpha = 0.02$ (soft pores), $\alpha = 0.12$ (semi-stiff pores) and $\alpha = 0.8$ (stiff pores).

Figure 5 displays the single-pore test results. The bulk and shear moduli of saturated rock are calculated using different rock-physics modelling methods with a single-pore aspect ratio. In both the water saturation and gas saturation models, the results of Hashin–Shtrikman bounds (black lines) and DEM model (blue lines) are considered as references to compare with the results of Kuster–Toksöz model (green points) and the proposed extended Xu–White model (red points). Note that the Kuster–Toksöz model results are close to the DEM model only when the porosity is smaller than the pore aspect ratio, and some points exceed the Hashin–Shtrikman lower bound. When the pore aspect ratio is close to 1, the Kuster–Toksöz model results are close to the Hashin–Shtrikman upper bound. The results obtained by the extended Xu–White model are sound, consistent well with the DEM results in the given porosity interval, and always within the Hashin–Shtrikman upper and lower bounds.

Figure 6 displays the multi-pore test result. The elastic moduli of saturated rock are calculated using the extended Xu–White model with different soft and stiff pore volumes along with the background semi-stiff pores. The red solid line represents rock moduli with only semi-stiff pores. The lower dashed green lines and the upper dashed blue lines indicate the increasing volume of soft pores and stiff pores, respectively. From both the water saturation and gas saturation models, we can observe that the bulk and shear moduli decrease with the increase in the soft pore volume and increase with the increase in the stiff pore volume. This rule is useful in the selection and adjustment of the rock-physics parameters in the real data application. In addition, the results are also consistent with the Hashin–Shtrikman upper and lower bounds within the given porosity range.

Application

Diagnostics of well-log data

Well-log data can effectively reflect the properties of rocks and pore fluids underground and are often used in the calibration and verification of rock-physics models. The quality of well logs has a significant influence on reservoir characteristics analysis and the establishment of rock-physics templates. Figure 7 displays the original well logs and interpreted log-facies for the target interval of a calibration

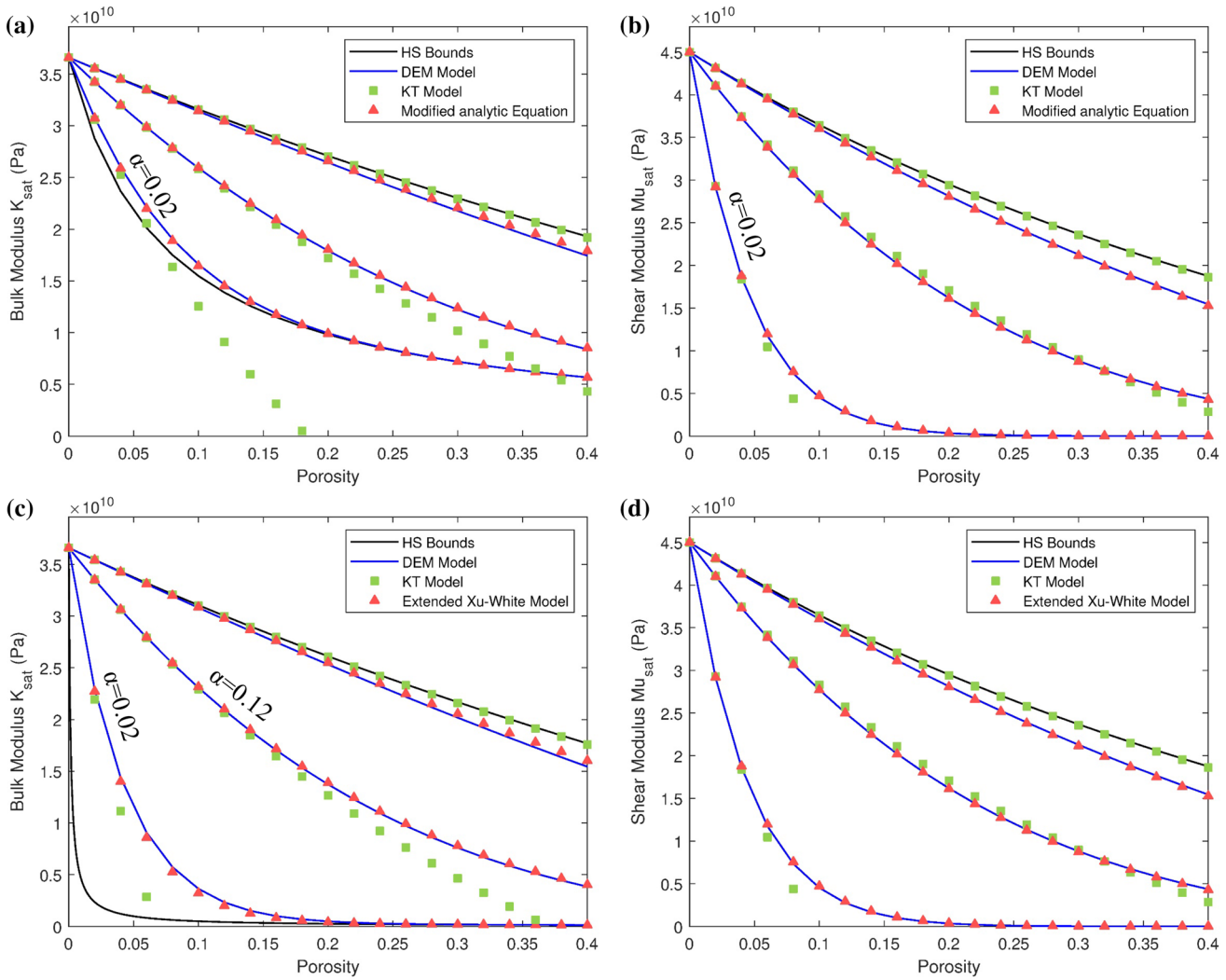

Fig. 5 Single-pore-saturated rock modelling with different pore aspect ratios, water-saturated bulk modulus (**a**) and shear modulus (**b**) versus porosity, gas-saturated bulk modulus (**c**) and shear modulus (**d**) versus porosity

well W1. The data set contains a complete set of well logs, including sonic logs (P- and S-wave velocities), a density log and petrophysical curves (porosity, shale volume and water saturation). Two main gas-bearing sandstone reservoirs are shown in yellow facies; their thicknesses are about 15 m and 20 m; and the average porosity inside the reservoir is approximately 13%. The original porosity curve in Fig. 7d is the effective porosity. Note that the shale layers have zero porosity and 100% shale volume values, as shown by the red arrows in Fig. 7. These values are not appropriate for rock-physics modelling. In addition, due to these zero porosity values, the crossplots of the effective porosity versus the P- and S-wave velocity in Fig. 8 show a messy distribution, especially the shale and siltstone points in the marked red ellipses. Thus, we need to estimate the total porosity before rock-physics modelling.

Since rock-physics models predict P- and S-wave velocities from the total porosity and shale volume, they can be used in an inversion mode to estimate a total porosity curve that matches the measured velocities. We use the extended Xu–White model to estimate the total porosity constrained by the measured P-wave velocity and compare the results with the conventional Xu–White model and density method. The estimated total porosity is then used in the prediction of the S-wave velocity. Because no constraint is imposed on the predicted S-wave velocity, the match between the predicted and measured S-wave velocities can reflect the reliability of the total porosity estimation result to some extent. The rock properties for the total porosity estimation using the extended Xu–White model and the conventional Xu–White model are listed in Table 1. Among them, the solid parameters (bulk modulus, shear modulus and density) and the pore aspect ratios are determined from the calibration of well W1;

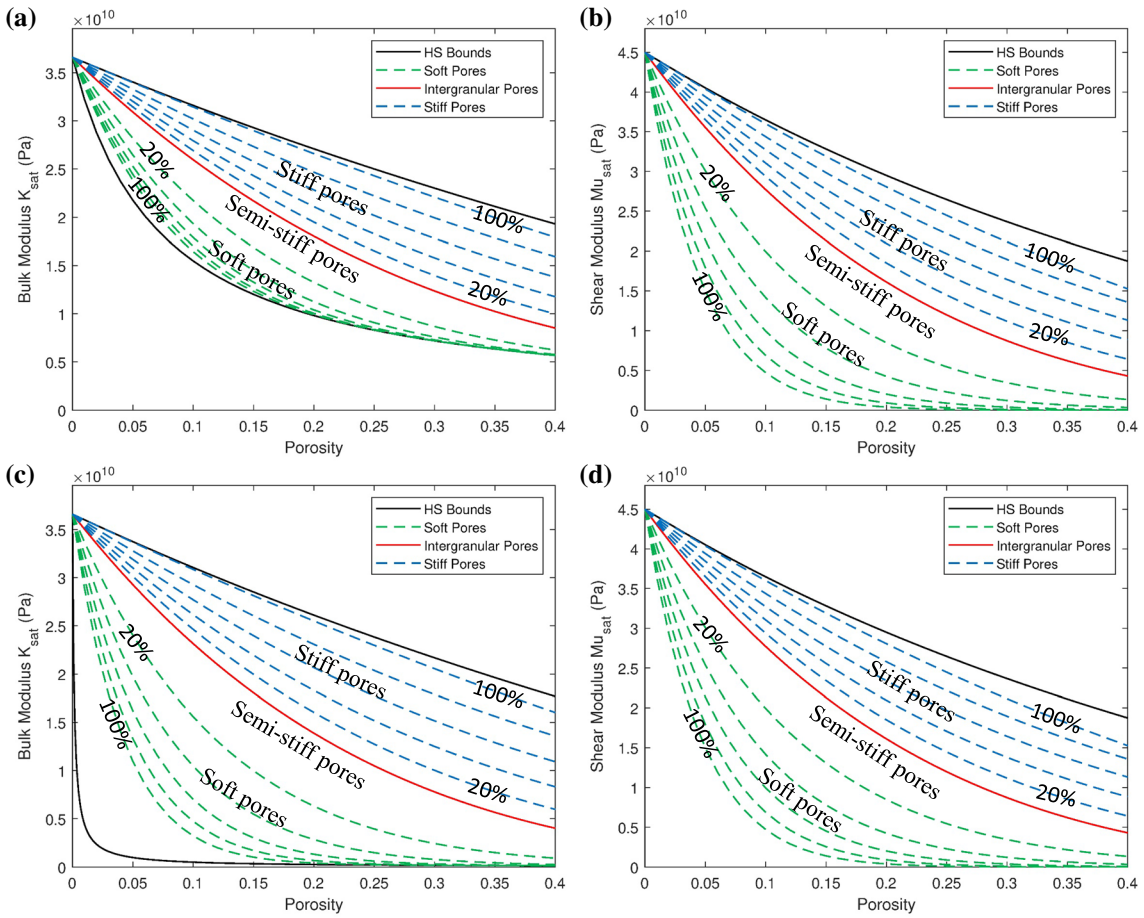

Fig. 6 Multi-pore-saturated rock modelling with different volumes of soft and stiff pores, water-saturated bulk modulus (**a**) and shear modulus (**b**) versus porosity, gas-saturated bulk modulus (**c**) and shear modulus (**d**) versus porosity

the fluid parameters are calculated by the Batzle–Wang formulas (1992) at a temperature of 170 °C and a pore pressure of 25 MPa for the target zone. In the extended Xu–White model, we consider three pore types, the intergranular semi-stiff pore, feldspar dissolution stiff pore and wet clay soft pore, while in the conventional Xu–White model, only two pore types, the semi-stiff pore and soft pore, are considered.

Figure 9a shows the corrected and original shale volume curves. The corrected curve is more reasonable as it does not contain 100% shale volume values, considering the existence of bound wet clay pores in shale layers. Figure 9b compares the estimated total porosity curves using the extended Xu–White model, conventional Xu–White model and density method. The density-estimated porosity (green) has values that exceed the general sandstone critical porosity; the extended Xu–White model result (red) is close to the conventional Xu–White model result (blue) overall but is more accurate at the sandstone reservoir locations, as the red arrows show. Figure 9c–e shows the comparisons of the predicted and measured P- and S-wave velocities and densities, using the total porosity estimated by the extended and conventional Xu–White models, respectively. Since the measured P-wave velocity is used as a constraint in the total porosity estimation, the predicted P-wave velocity curves overlap with each other as expected. The S-wave velocity predicted by the extended Xu–White model (red) matches better with the measured S-wave velocity (black) than the conventional Xu–White model result (blue), which indicates that the total porosity estimated by the extended model is more reliable. In addition, the predicted density provides a more realistic value than the original density at the location where the calliper log shows an expansion in Fig. 9f.

Furthermore, we replace the original effective porosity of the crossplots in Fig. 8 with the estimated total porosity by the extended Xu–White model, as shown in Fig. 10. Note that the crossplots show clear rock-physics characteristics in this case. The scattered data points of different lithologies distributed regularly between the theoretical clean sandstone line and pure shale line, and the shale volume trend is consistent with the log interpretation results, as the black arrows indicate.

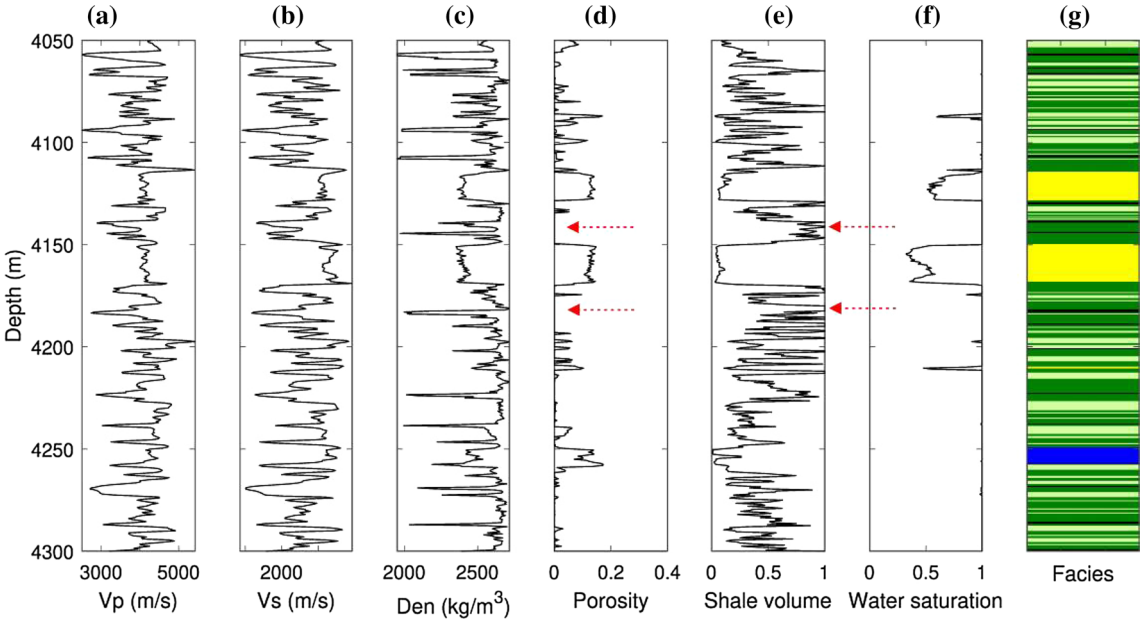

Fig. 7 Original log data of well W1. **a** P-wave velocity; **b** S-wave velocity; **c** density; **d** porosity; **e** shale volume; **f** water saturation; **g** facies defined by well-log interpretation. In the facies profile, shale is dark green, siltstone is light green, the coal formation is black, the water-saturated sandstone is blue, and the gas-bearing sandstone is yellow

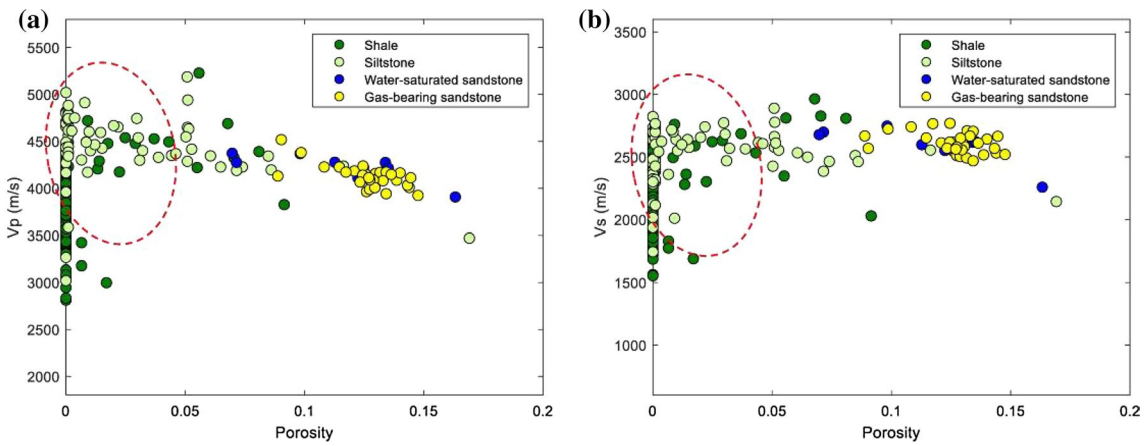

Fig. 8 Crossplots of P-wave velocity (**a**) and S-wave velocity (**b**) versus the original effective porosity from well W1

Table 1 Rock-physics model parameters for total porosity estimation

Lithology or fluid	Bulk modulus (GPa)	Shear modulus (GPa)	Density (g/cm^3)	Pore type	Pore aspect ratio
Sand	43.00	32.00	2.66	Semi-stiff	0.12
				Stiff	0.60
Clay	25.00	9.00	2.58	Soft	0.05
Water	2.33	0.00	0.95		
Gas	0.05	0.00	0.14		

The extended Xu–White model uses the semi-stiff, stiff and soft pores, while the conventional Xu–White model uses only the semi-stiff and soft pores

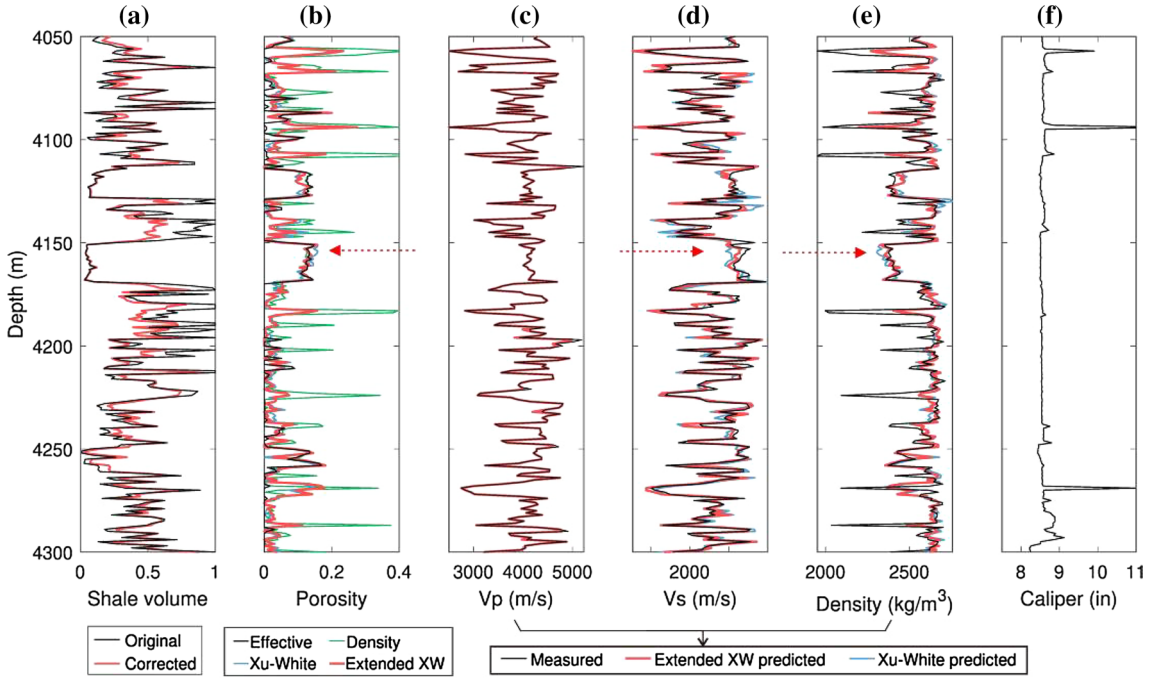

Fig. 9 Total porosity estimation-related curves. **a** Shale volume; **b** porosity; **c** P-wave velocity; **d** S-wave velocity; **e** density; **f** calliper log. The measured P-wave velocity is used as a constraint to invert the total porosity, and the measured S-wave velocity is used as a reference to test the total porosity estimation result

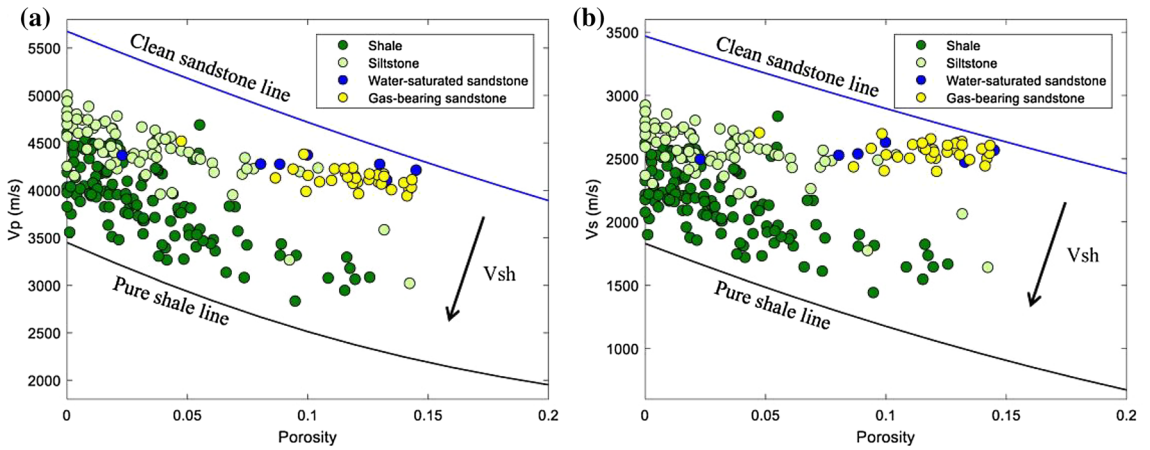

Fig. 10 Crossplots of P-wave velocity (**a**) and S-wave velocity (**b**) versus the estimated total porosity. The blue line and black line represent the theoretical clean sand line and the pure shale line, respectively. The black arrows indicate the increasing direction of the shale volume

Establishment and verification of rock-physics template

Rock-physics templates (RPTs) are charts or templates of rock-physics models for the interpretation of lithology and hydrocarbons (Ødegaard and Avseth 2004; Chi and Han 2009; Avseth et al. 2010). RPTs consist of crossplots of seismic parameters (e.g. acoustic impedance vs. Vp/Vs ratios), which allow us to perform the rock-physics analysis of both well data and elastic inversion results.

Figure 11 displays the crossplots of acoustic impedance versus Vp/Vs ratios for the target zone of the calibration well W1, superimposed with RPT generated from the extended Xu–White model using the previous rock parameters in Table 1. The porosity range is set from 0 to 20%, and the shale volume and the water saturation ranges are set from 0 to 100%. Their variation trends are shown by arrows in each

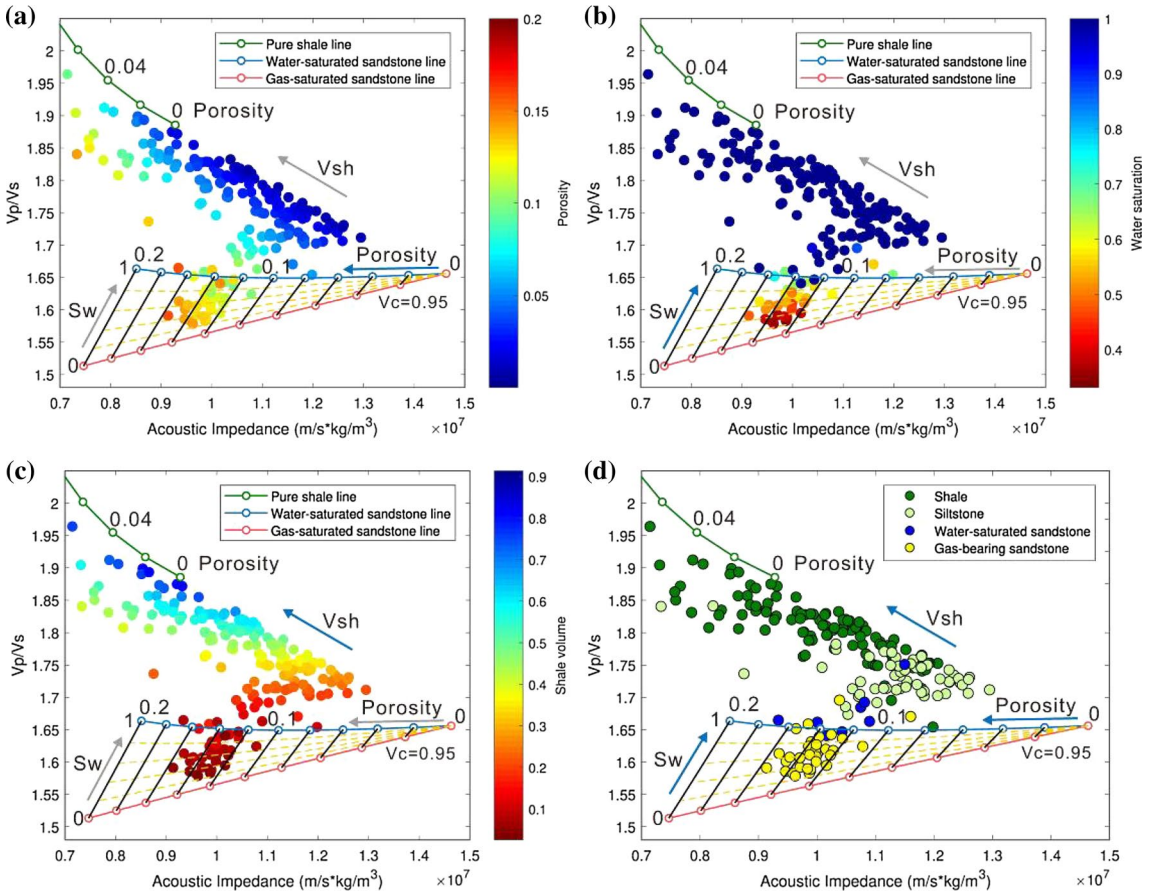

Fig. 11 Acoustic impedance versus Vp/Vs crossplots of well-log data from calibration well W1 superimposed with the modelled RPT and colour-coded by: **a** porosity, **b** water saturation, **c** shale volume and **d** well-log interpretation conclusions

crossplot of Fig. 11. The green solid line represents pure shale; the blue and red solid lines represent water- and gas-saturated sandstone with 5% clay content, respectively; and the black solid lines and the yellow dotted lines represent isolines of porosity and water saturation, respectively. Note that the RPT-indicated porosity for the data points in the reservoir zone is approximately 10–15%, which is consistent with the porosity shown by the colour-coded values of these points in Fig. 11a. The RPT-indicated water saturation and shale volume are also consistent with the corresponding colour-coded values in Fig. 11b, c. In addition, in Fig. 11d, we observe that the artificial log-interpreted gas-bearing sandstone points almost fall in the reservoir zone, and the water-saturated sandstone, siltstone and shale points sit just between the theoretical water-saturated sandstone line and pure shale line.

Our rock-physics model uses patchy distribution to calculate fluid-saturated rock moduli, as previously mentioned. For comparison, we here assume a uniform distribution of fluid in the RPT modelling. The result is shown in Fig. 12. Note that the main difference in Figs. 11b and 12 is the water saturation of the template. In the patchy distribution

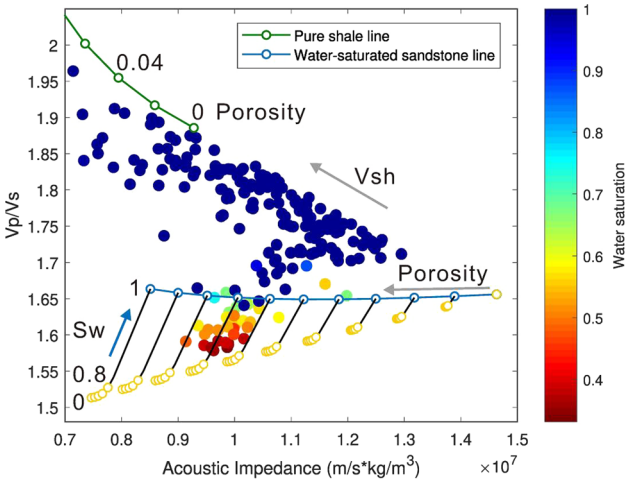

Fig. 12 Acoustic impedance versus Vp/Vs crossplots of well-log data from calibration well W1 superimposed with the comparative RPT using uniform fluid distribution and colour-coded by water saturation

mode, the elastic properties show a more linear change with increasing gas saturation, as shown by the yellow dotted lines in Fig. 11b, while in the uniform distribution mode,

a small amount of gas will cause almost the same elastic properties as the commercial amount of gas, as shown by the yellow circles in Fig. 12. In addition, the RPT-indicated minimum water saturation under the uniform distribution assumption is approximately 80%, which is not consistent with the minimum colour-coded values of data points, which is approximately 35%. This demonstrates that the patchy distribution assumption of the fluid saturation mode tends to be more suitable than the uniform distribution in our case.

To investigate the scale effect on the RPT, we apply a moving-window Backus averaging method (Lindsay and Van Koughnet 2001) to upscale the log curves to seismic scale in Fig. 13. The size of the upscaling window at a certain depth is dynamically determined by estimating the temporal wavelength from a chosen upscaling frequency and the velocity at that depth. The upscaling frequency here is set to 100 Hz according to the bandwidth of the seismic inversion results. Note that the ranges of the P- and S-wave velocity and density curves decrease substantially in Fig. 13 due to the filtering effect of the Backus average. After this, the scattered data points in Fig. 14 are transformed to the seismic scale. We observe that the best-fit template clay content value decreases from 0.95 to 0.85 when the data points upscale from the well-log scale to the seismic scale.

Then, a verification well, W2, is selected to verify the reliability of the template. Figure 15 displays the crossplots

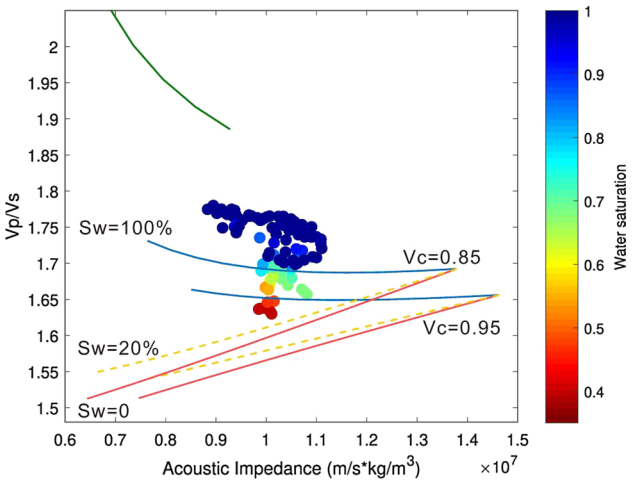

Fig. 14 Acoustic impedance versus Vp/Vs crossplots of seismic-scale log data in Fig. 13 superimposed with RPTs with different clay contents and colour-coded by water saturation

of the acoustic impedance versus Vp/Vs ratios for the target interval of the verification well W2, superimposed with the same RPT calibrated by well W1 at the well-log scale. Note that the template-indicated gas-bearing sandstone porosity range (10–14%), minimum water saturation (50%) and shale volume trend are consistent with the colour-coded values of scattered data points. In addition, the upscaled data points

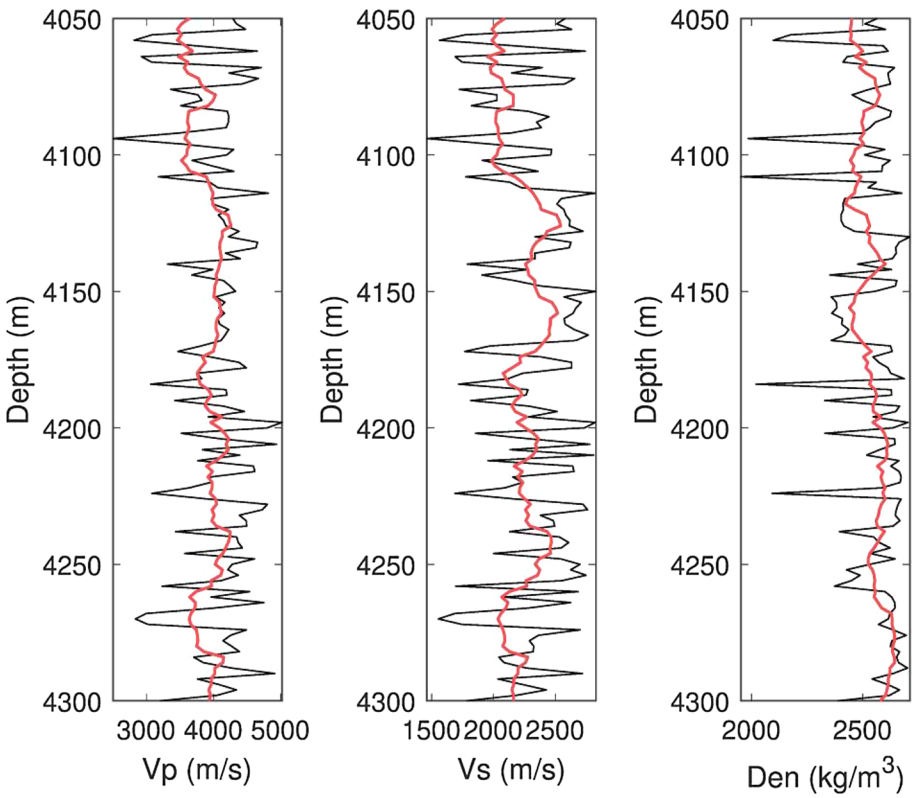

Fig. 13 Backus average upscaling of well-log data; the black curves represent the original log data, and the red curves represent seismic-scale log data

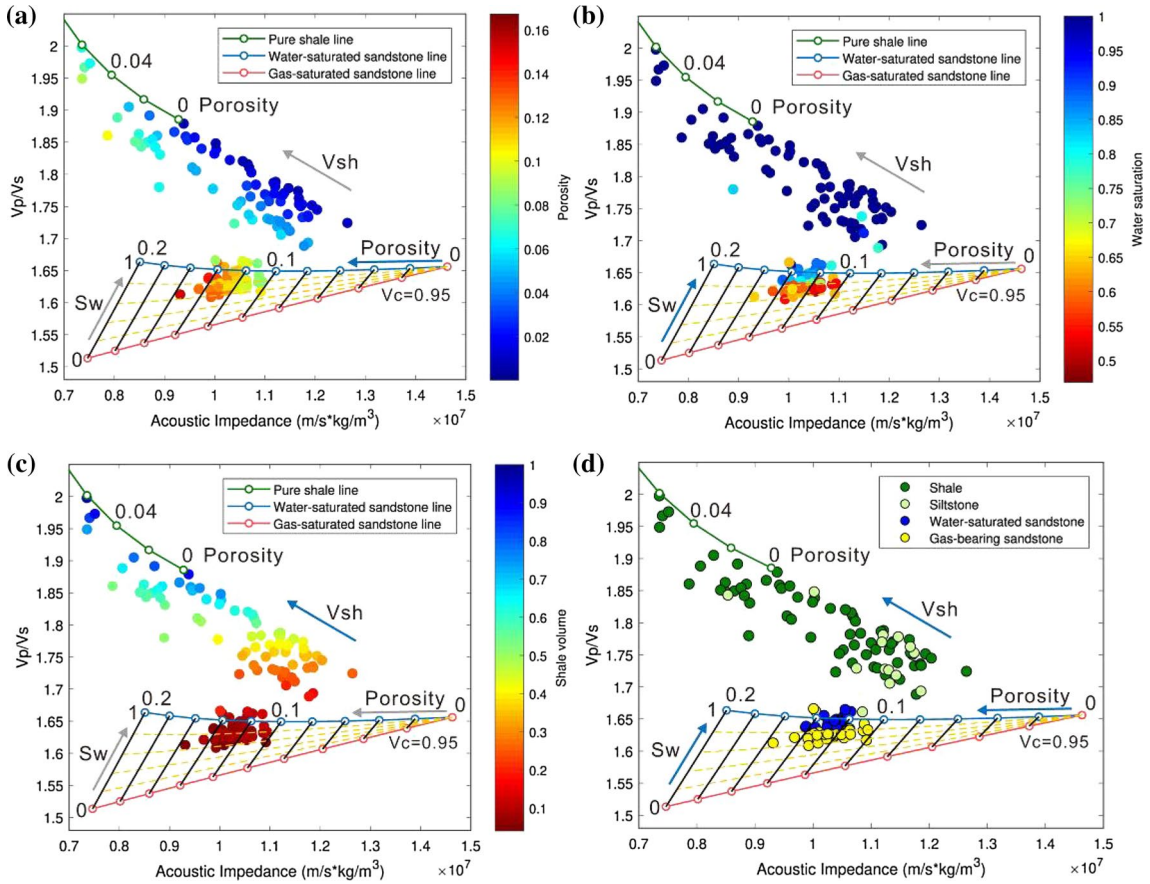

Fig. 15 Acoustic impedance versus Vp/Vs crossplots of well-log data from verification well W2 superimposed with the same rock-physics template calibrated by well W1 and colour-coded by: **a** porosity, **b** water saturation, **c** shale volume and **d** well-log interpretation conclusions

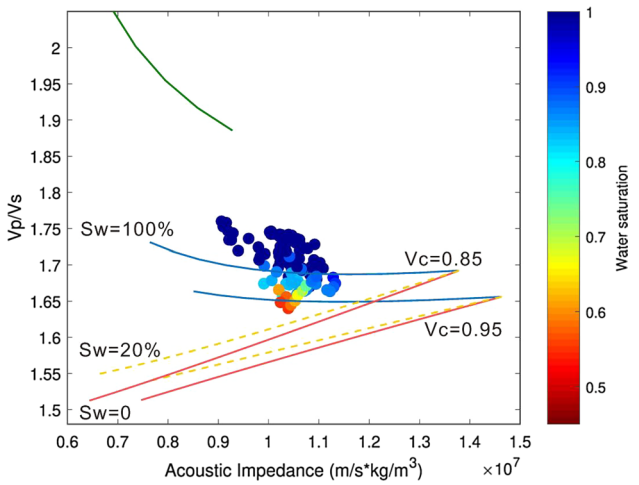

Fig. 16 Acoustic impedance versus Vp/Vs crossplots of seismic-scale log data from verification well W2 superimposed with RPTs with different clay contents and colour-coded by water saturation

in Fig. 16 also match well with the seismic-scale template in which the clay content is equal to 0.85. These demonstrate a good validity of the established RPT at both the well-log and the seismic scales.

Porosity and gas saturation prediction

In the following section, we apply the established RPT to predict the porosity and gas saturation of deep-buried sandstone reservoirs from the prestack seismic data. Figure 17 displays three partial angle stack seismic sections passing through well W1 which is located at CDP 1071. The inserted well synthetic seismic records in each section are calculated from the elastic parameters (P- and S-wave velocity and density) of well-log data and a 30-Hz zero-phase Ricker wavelet using the Aki and Richards equation (2002) with the corresponding average incident angles of 9°, 15°, 21°. Note that the synthetic seismic records match well with the real seismic data and has an obvious amplitude-versus-angle (AVA) response at the gas layers. The seismic amplitude decreases as the incidence angle increases, which can also be observed from the

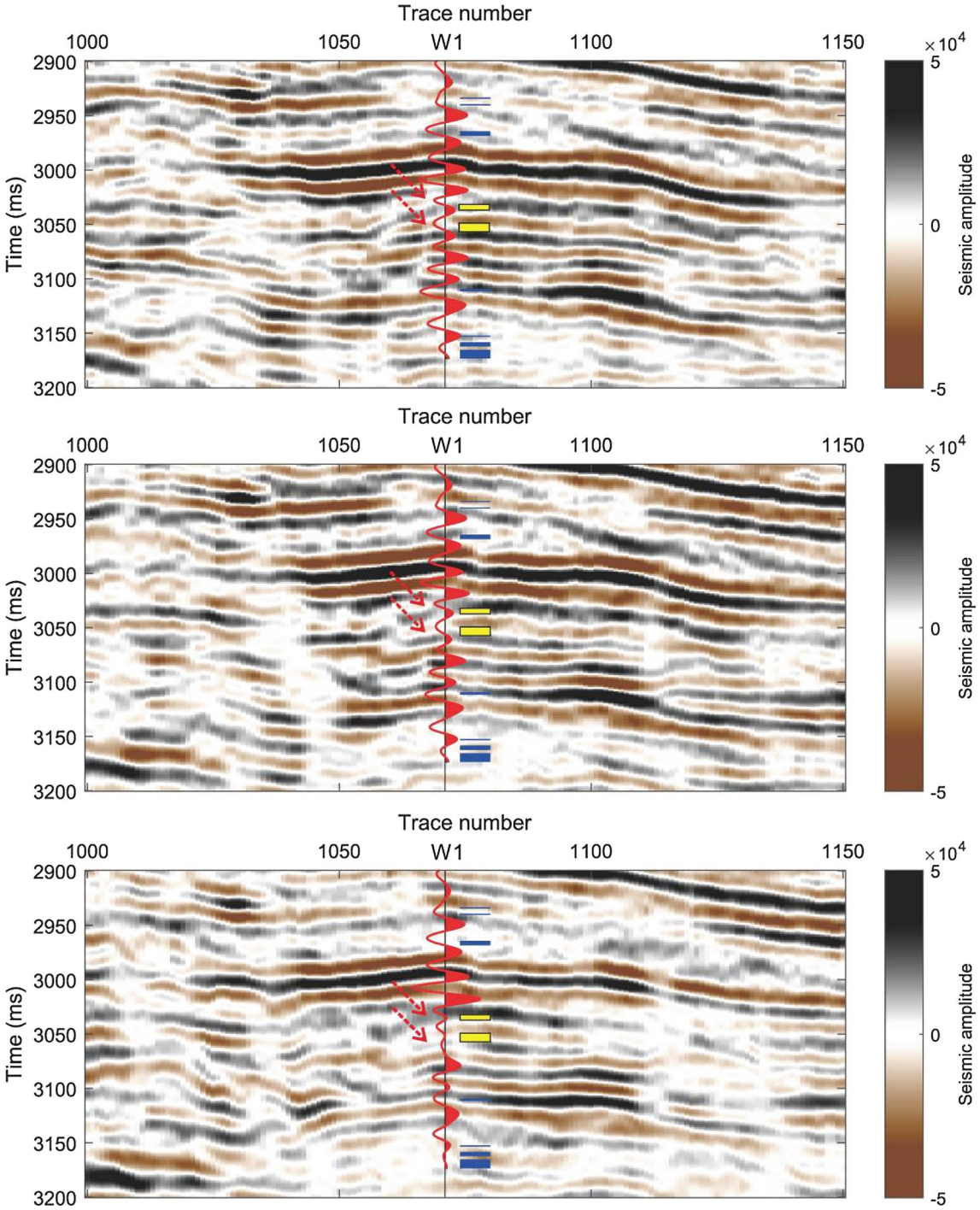

Fig. 17 Partial angle stack seismic sections crossing well W1 with average incident angles of 9°, 15°, 21°, respectively. The inserted well curve represents the calibrated synthetic seismic records generated by the corresponding average incident angles; the reservoir interpretation results are displayed on the right side; yellow rectangle represents gas sand and blue rectangles represent brine sand

borehole-side seismic data. Figure 18 shows the acoustic impedance and Vp/Vs inversion results for the seismic line in Fig. 17 using the Bayesian linearized AVO inversion (Buland and Omre 2003). Arrows indicate two gas-bearing sandstone reservoirs with medium acoustic impedance and low Vp/Vs values. Note that we can only roughly estimate the locations of two gas layers just from the inversion results. However, with the RPT, we can further estimate

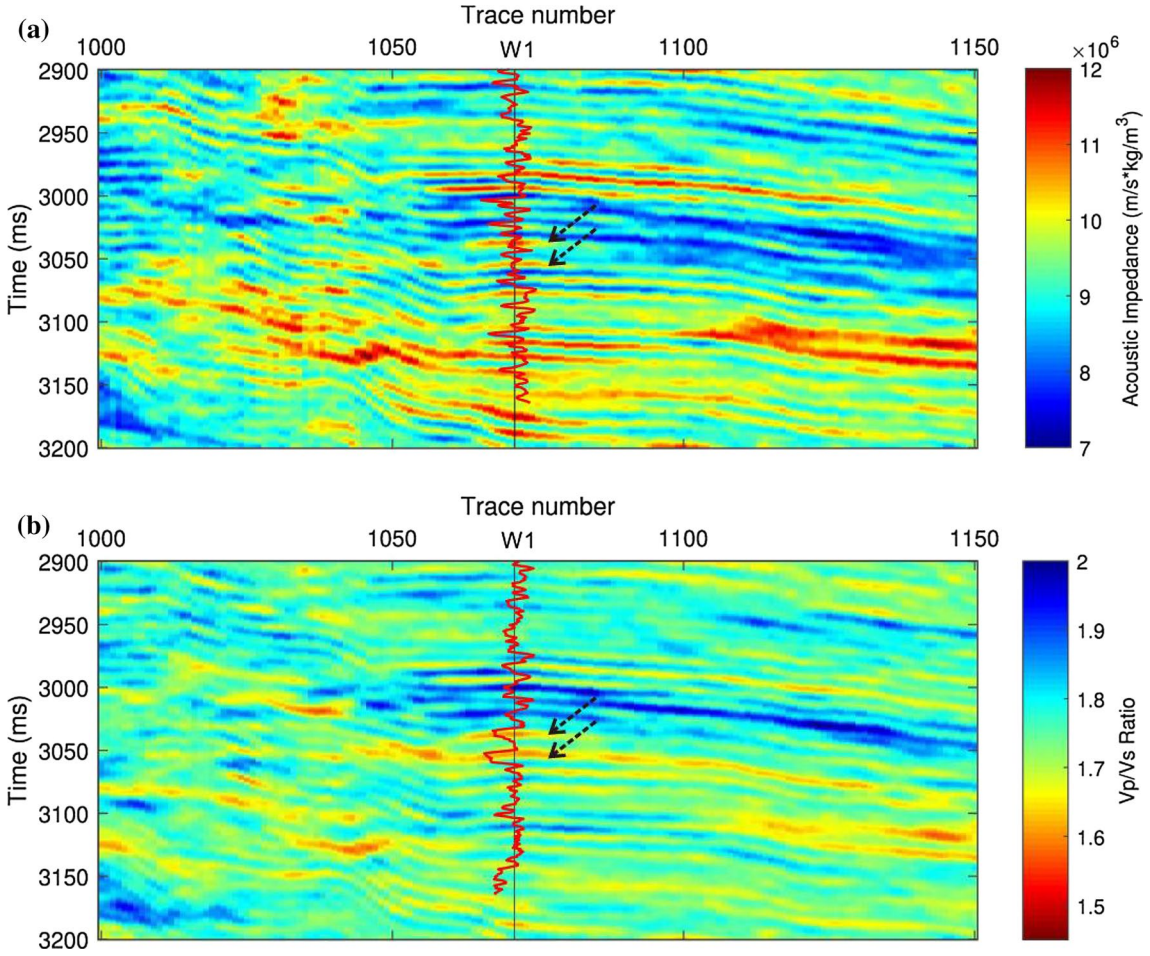

Fig. 18 Prestack seismic inversion results of acoustic impedance (**a**) and Vp/Vs (**b**) with the corresponding log cures inserted. Arrows indicate the locations of two gas reservoirs in well W1

the porosity and gas saturation of gas-bearing sandstone reservoirs.

Figure 19 displays the projection of the acoustic impedance and Vp/Vs data pairs onto the seismic-scale RPT. These projection points are relatively concentrated due to the limited frequency bandwidth of the seismic inversion data. Points that fall in the reservoir zone are defined as sandstone reservoirs. In addition, based on the position of these projection data points, we can directly transform the acoustic impedance and Vp/Vs data pairs into the porosity and gas saturation data pairs. The porosity and gas saturation of points that fall outside the reservoir zone are set to zero. That is to say, we only focus on the porosity and gas saturation of sandstone reservoirs and ignore that of shale or siltstone. Figure 20 shows the prediction results of the porosity and gas saturation. Note that the predicted porosity and gas saturation are in good agreement with the well-log data. These results demonstrate the validity of the improved rock-physics model and can be used as a guidance for the further deep-buried gas reservoir exploration in this area.

Discussion

A practical workflow for rock-physics modelling of deep-buried sandstone gas reservoirs with complex pore structures has been proposed. For clay–sand mixture layers, the Xu–White model can estimate both P- and S-wave

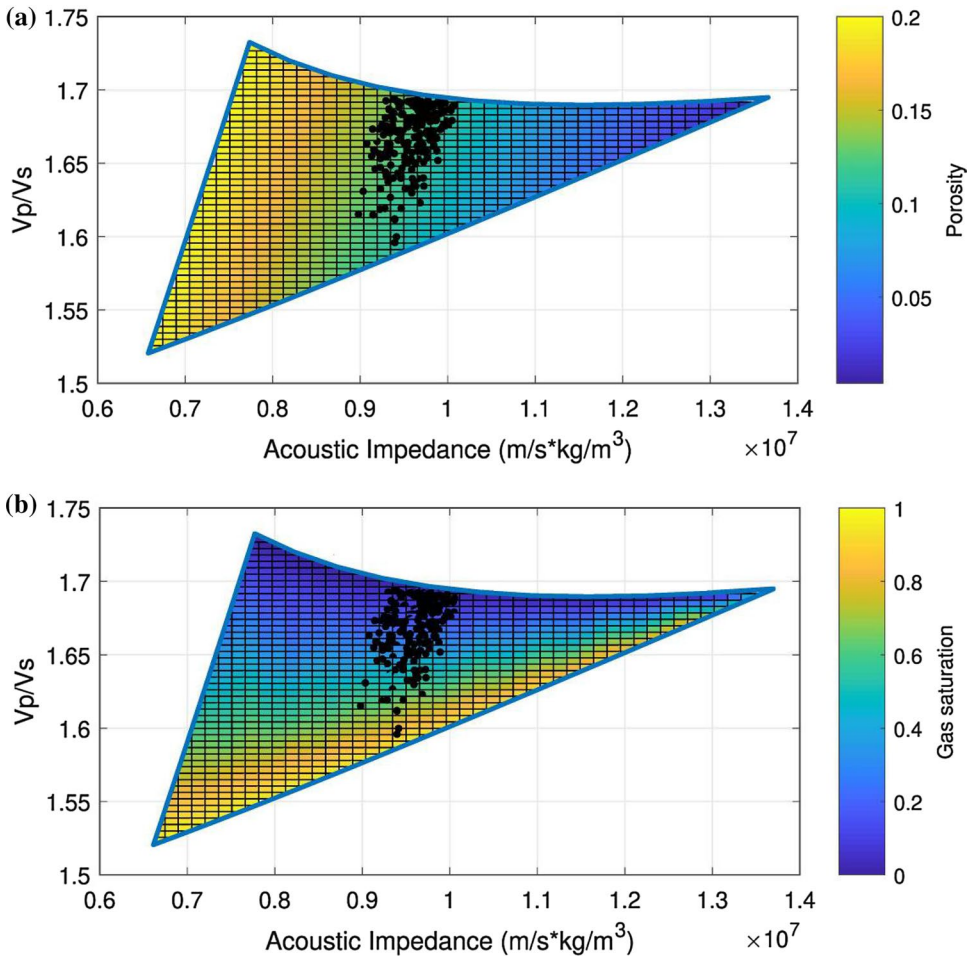

Fig. 19 Reservoir zone in seismic-scale RPT colour-coded by template-indicated porosity (**a**) and gas saturation (**b**); the projected black points represent acoustic impedance and the Vp/Vs data pairs from the seismic inversion

velocities over the full range of siliciclastic rocks from clean sandstones to pure shales, whether consolidated or moderately unconsolidated (Xu and White 1996). We extend the Xu–White model, originally accounts for two pore types (wet clay soft pore and quartz intergranular semi-stiff pores), to our case by introducing a third feldspar-related dissolution stiff pore. Our extended Xu–White model consists of three steps: (1) rock matrix modelling using time-average equations; (2) dry rock modelling using a multi-pore analytical approximation; and (3) fluid-saturated rock modelling using patchy saturation.

The input parameters required by the extended Xu–White model include the elastic moduli and densities of mineral particles and pore fluids, the porosity and shale volume of the rock frame, and three pore aspect ratios for three types of pores. For mixed minerals, the elastic moduli and density of clays are variable and not very well known, leading to uncertainties in the rock matrix modelling. The estimation of these parameters relies on careful calibration of well logs through trial-and-error experiments. In practice, the parameters calibration process has certain rules to follow; that is, the mineral moduli and density control the overall adjustment of the predicted P- and S-wave velocity and density curves, while the pore aspect ratios act as a local adjustment, in which larger pore aspect ratios correspond to higher values of predicted velocities. Utilizing these rules can make the calibration process easier. When the predicted curves match well with the measured logs, we can determine these input rock-physics modelling parameters.

In dry rock modelling, by assuming a constant dry rock Poisson's ratio, we decouple the differential effective medium equations and then derive a multi-pore analytical approximation for the dry rock moduli calculation. Despite this assumption, we note that the Poisson's ratio derived from the multi-pore dry rock approximation in Eqs. (18) and (19) is not constant. In fact, the constant assumption is not a rigorous restriction to the dry rock Poisson's ratio, because we only apply this assumption in the calculation of geometry parameters P_i and Q_i, and the final expressions of dry rock moduli are still related to porosity. In addition, to force the dry rock Poisson's ratio to be constant will result in a poor approximation for the shear-wave velocity (Keys and Xu 2002). On the other hand, for rock-physics templates in Fig. 11, note that Vp/Vs varies with porosity, especially for

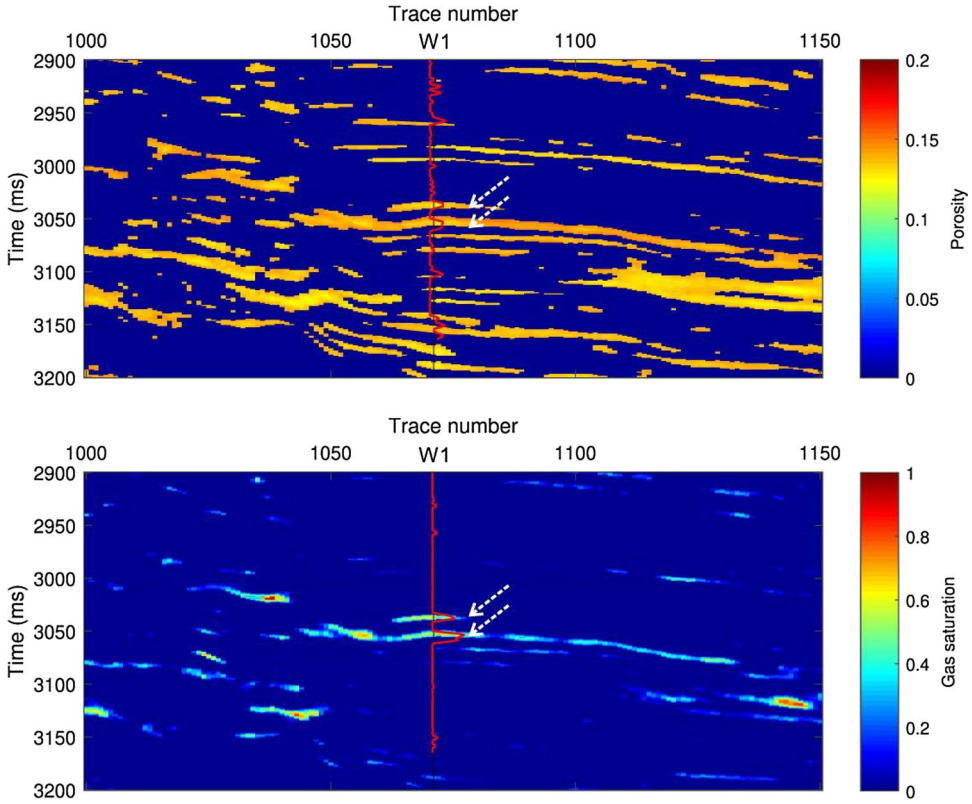

Fig. 20 Prediction results of porosity (**a**) and gas saturation (**b**) for deep-buried sandstone reservoirs with corresponding porosity and gas saturation log curves inserted

the gas-saturated sandstone model. However, also note that the increase in clay content will cause a more drastic variation of Vp/Vs, because the rock matrix is more sensitive to the clay content variation than the high-porosity rocks (Avseth et al. 2010). This means that the variation degree of Vp/Vs depends on the clay content of the rock matrix. Therefore, when sandstone contains clay, the dry rock Poisson's ratio will change with porosity, which also indicates that the dry rock Poisson's should not be forced to be constant.

The clay content in sandstone is also an important parameter related to the scale effect, reservoir heterogeneity and saturation distribution (Jakobsen et al. 2003b). For thin-interbedded sand and shale layers, upscaling means an increase in the intercalating shale, which, in turn, increases reservoir heterogeneity and thus affects the fluid saturation distribution pattern. At the well-log scale, the reservoir sandstone data in the studied wells match nicely with the template when the clay content is 0.95, which is basically consistent with the shale volume log curve values at sandstone locations. When upscaling to the seismic scale using the Backus average, the P- and S-wave velocity and density curves become smooth and concentrated, and the best-fit clay content value for the template changes. A different upscaling frequency corresponds to a different best-fit template, which leads to uncertainties in seismic interpretation. In our case, we set the upscaling frequency based on the frequency band of seismic inversion results. Both the observations at the well-log scale and the seismic scale are consistent with a patchy-saturation behaviour. One possible explanation is that the heterogeneities caused by clay content in sandstone control the saturation pattern, even in seismic scale, the seismic wave may experience patchy saturation when the thickness of clay–sand mixture layer is relatively large (Avseth et al. 2010).

In addition to the two main uncertainties associated with the above-mentioned clay properties, the extended Xu–White model is also limited by several basic assumptions inherited from the DEM model such as the isotropic, linear, and elastic rock and idealized ellipsoidal pore geometries (Mavko et al. 2009). Besides, we have not considered uncertainties caused by shale-related anisotropy and fluid-flow-related dispersion and attenuation, which will be investigated in future research to obtain a better model. Despite these uncertainties, we have found that the extended Xu–White model is useful for modelling deep-buried sandstone reservoirs, and it can also be applied to other types of rocks which have complex pore structures, such as carbonate rock.

Conclusions

We have proposed an improved rock-physics model for deep-buried sandstone reservoirs based on the geological characteristics analysis. This model can handle complex pore structure rocks with high computational efficiency compared to the differential effective medium theory. It has been used in total porosity estimation and S-wave velocity prediction; the results show that our model is more accurate than the density method and the conventional Xu–White model, which considers only two pore types. The rock-physics template generated by the extended Xu–White model provides a very useful tool for the porosity and gas saturation prediction of deep-buried gas reservoirs. The template needs to be carefully calibrated and validated by well-log data while honouring local geologic factors. The reliability of the template depends on the input data quality and the model assumptions. Moreover, the scale effects on the template should be considered when we move from the well-log scale to the seismic scale. Nevertheless, the established rock-physics template shows good performance in the porosity and saturation prediction of gas reservoirs and can help reduce risk in the deep seismic exploration and prospect evaluation.

Acknowledgements This work was financially supported by the Natural Science Foundation of China (41674139) and the National Science and Technology Major Project (2016ZX05033-02). We thank the Sinopec Shanghai branch for data provided and permission to publish the results of this research. Yaneng Luo would also like to thank the Basin and Reservoir Studies (BRS) group at University of Bergen for hospitality and support during his one-year visit.

Compliance with ethical standards

Conflict of interest On behalf of all authors, the corresponding author states that there is no conflict of interest.

References

Aki K, Richards PG (2002) Quantitative seismology, 2nd edn. University Science Books, California

Avseth P, Mukerji T, Mavko G (2005) Quantitative seismic interpretation: Applying rock physics tools to reduce interpretation risk. Cambridge University Press, New York

Avseth P, Mukerji T, Mavko G, Dvorkin J (2010) Rock-physics diagnostics of depositional texture, diagenetic alterations, and reservoir heterogeneity in high-porosity siliciclastic sediments and rocks—a review of selected models and suggested work flows. Geophysics 75(5):A31–A47

Avseth P, Johansen TA, Bakhorji A, Mustafa HM (2014) Rock-physics modelling guided by depositional and burial history in low-to-intermediate-porosity sandstones. Geophysics 79(2):D115–D121

Bachrach R, Avseth P (2008) Rock physics modeling of unconsolidated sands: accounting for nonuniform contacts and heterogeneous stress fields in the effective media approximation with applications to hydrocarbon exploration. Geophysics 73(6):E197–E209

Bai J, Yue C, Liang Y, Song Z, Ling S (2013) Variable aspect ratio method in the Xu–White model for shear-wave velocity estimation. J Geophys Eng 10:1–6

Batzle M, Wang Z (1992) Seismic properties of pore fluids. Geophysics 57:1396–1408

Berge PA, Berryman JG, Bonner BP (1993) Influence of microstructure on rock elastic properties. Geophys Res Lett 20:2619–2622

Berryman JG (1992) Single-scattering approximations for coefficients in Biot's equations of poroelasticity. J Acoust Soc Am 91:551–571

Berryman JG, Pride SR, Wang HF (2002) A differential scheme for elastic properties of rocks with dry or saturated cracks. Geophys J Int 151:597–611

Best A (2014) Physics of rocks for hydrocarbon exploration: introduction. Geophys Prospect 62:1203–1204

Bosch M, Carvajal C, Rodrigues J, Torres A, Aldana M, Sierra JS (2009) Petrophysical seismic inversion conditioned to well-log data: methods and application to a gas reservoir. Geophysics 74(2):O1–O15

Buland A, Omre H (2003) Bayesian linearized AVO inversion. Geophysics 68:185–198

Buland A, Kolbjørnsen O, Hauge R, Skjæveland Ø, Duffaut K (2008) Bayesian lithology and fluid prediction from seismic prestack data. Geophysics 73(3):C13–C21

Cao Q, Zhou W, Liu Y, Chen W, Ji A, Lu J, Wang Y (2017) Characteristics and origin of deep high-porosity zones in slope of Xihu Sag. J Cent South Uni (Sci Technol) 48:751–760

Cheng C, Toksöz MN (1979) Inversion of seismic velocities for the pore aspect-ratio spectrum of a rock. J Geophys Res 84:7533–7543

Chi X, Han D (2009) Lithology and fluid differentiation using rock physics template. Lead Edge 28:60–65

Dutton SP, Loucks RD (2010) Diagenetic controls on evolution of porosity and permeability in lower Tertiary Wilcox sandstones from shallow to ultradeep (200–6700 m) burial, Gulf of Mexico Basin, U.S.A. Mar Pet Geol 27:69–81

Dvorkin J, Nur A (1996) Elasticity of high-porosity sandstones: theory for two North Sea data sets. Geophysics 61:1363–1370

Dyman TS, Wyman RE, Kuuskraa VA, Lewan MD, Cook TA (2003) Deep natural gas resources. Nat Resour Res 12:41–56

Guéguen Y, Palciauskas V (1994) Introduction to the physics of rocks. Princeton University Press, Chichester

Hu M, Shen J, Hu D (2013) Reservoir characteristics and its main controlling factors of the Pinghu Formation in Pinghu structural belt, Xihu depression. Oil Gas Geol 34:185–191

Jakobsen M, Hudson J, Johansen TA (2003a) T-matrix approach to shale acoustics. Geophys J Int 154:533–558

Jakobsen M, Johansen TA, McCann C (2003b) The acoustic signature of fluid flow in complex porous media. J Appl Geophys 54:219–246

Johansen TA, Drottning Lecomte I, Ystdal HG (2002) An approach to combined rock physics and seismic modelling of fluid substitution effects. Geophys Prospect 50:119–137

Keys RG, Xu S (2002) An approximation for the Xu–White velocity model. Geophysics 67:1406–1414

Keys R, Matava T, Foster D, Ashabranner D (2017) Isotropic and anisotropic velocity model building for subsalt seismic imaging. Geophysics 82(3):S247–S258

Kuster GT, Toksöz MN (1974) Velocity and attenuation of seismic waves in two-phase media. Geophysics 39:587–618

Lai J, Wang G, Fan Z, Chen J, Wang S, Zhou Z, Fan X (2016) Insight into the pore structure of tight sandstones using NMR and HPMI measurements. Energy Fuels 30:10200–10214

Lai J, Wang G, Chai Y, Xin Y, Wu Q, Zhang X, Sun Y (2017) Deep burial diagenesis and reservoir quality evolution of high-temperature, high-pressure sandstones: examples from Lower Cretaceous

Bashijiqike Formation in Keshen area, Kuqa depression, Tarim basin of China. AAPG Bull 101(6):829–862
Lai J, Wang G, Wang S, Cao J, Li M, Pang X, Zhou Z, Fan X, Dai Q, Yang L, He Z, Qin Z (2018) Review of diagenetic facies in tight sandstones: diagenesis, diagenetic minerals, and prediction via well logs. Earth Sci Rev 185:234–258
Li H, Zhang J (2012) Analytical approximations of bulk and shear moduli for dry rock based on the differential effective medium theory. Geophys Prospect 60:281–292
Lindsay R, Van Koughnet R (2001) Sequential Backus averaging: upscaling well logs to seismic wavelengths. Lead Edge 20:188–191
Mavko G, Mukerji T, Dvorkin J (2009) The rock physics handbook tools for seismic analysis of porous media, 2nd edn. Cambridge University Press, New York
Morad S, Al-Ramadan K, Ketzer JM, DeRos LF (2010) The impact of diagenesis on the heterogeneity of sandstone reservoirs: a review of the role of depositional facies and sequence stratigraphy. AAPG Bull 94(8):1267–1309
Müller TM, Gurevich B, Lebedev M (2010) Seismic wave attenuation and dispersion resulting from wave-induced flow in porous rocks—a review. Geophysics 75(5):A147–A164
Norris AN (1985) A differential scheme for the effective moduli of composites. Mech Mater 4:1–16
Ødegaard E, Avseth P (2004) Well log and seismic data analysis using rock physics templates. First Break 23:37–43
Pang X, Jia C, Wang W (2015) Petroleum geology features and research developments of hydrocarbon accumulation in deep petroliferous basins. Pet Sci 12:1–53
Rezaee R, Saeedi A, Clennell B (2012) Tight gas sands permeability estimation from mercury injection capillary pressure and nuclear magnetic resonance data. J Petrol Sci Eng 88–89:92–99
Ruiz F, Dvorkin J (2009) Sediment with porous grains: rock-physics model and application to marine carbonate and opal. Geophysics 74(1):E1–E15
Sun L, Zou C, Zhu R, Zhang Y, Zhang S, Zhang B, Zhu G, Gao Z (2013) Formation, distribution and potential of deep hydrocarbon resources in China. Pet Explor Dev 40:687–695
Vernik L, Kachanov M (2010) Modelling elastic properties of siliciclastic rocks. Geophysics 75(6):E171–E182
Wang S, Yuan S, Wang T, Gao J, Li S (2018) Three-dimensional geosteering coherence attributes for deep-formation discontinuity detection. Geophysics 83(6):O105–O113
White JE (1975) Computed seismic speeds and attenuation in rocks with partial gas saturation. Geophysics 40:224–232
Wu J, Zhang L, Wan L, Zhao Q, Yang C, Wang Y (2017) Provenance analysis of Pinghu Formation in Xihu sag. China Pet Explor 22:50–57
Wyllie MRJ, Gregory AR, Gardner LW (1956) Elastic wave velocities in heterogeneous and porous media. Geophysics 21:41–70
Xu S, Payne MA (2009) Modelling elastic properties in carbonate rocks. Lead Edge 28:66–74
Xu S, White RE (1995) A new velocity model for clays and mixtures. Geophys Prospect 43:91–118
Xu S, White RE (1996) A physical model for shear-wave velocity prediction. Geophys Prospect 44:687–717
Yuan S, Ji Y, Shi P, Zeng J, Gao J, Wang S (2019a) Sparse Bayesian learning-based seismic high-resolution time-frequency analysis. IEEE Geosci Remote Sens Lett. https://doi.org/10.1109/lgrs.2018.2883496
Yuan S, Liu Y, Zhang Z, Luo C, Wang S (2019b) Prestack stochastic frequency-dependent velocity inversion with rock-physics constraints and statistical associated hydrocarbon attributes. IEEE Geosci Remote Sens Lett 16:140–144
Zhao L, Nasser M, Han D (2013) Quantitative geophysical pore-type characterization and its geological implication in carbonate reservoirs. Geophys Prospect 61:827–841
Zimmerman RW (1985) The effect of microcracks on the elastic moduli of brittle materials. J Mater Sci Lett 4:1457–1460
Zou C, Zhu R, Liu K, Su L, Bai B, Zhang X, Yuan X, Wang J (2012) Tight gas sandstone reservoirs in China: characteristics and recognition criteria. J Pet Sci Eng 88–89:82–91